Solvent-free self-assembly synthesis of N-doped ordered mesoporous carbons as effective and bifunctional materials for CO2 capture and oxygen reduction reaction

Xu Liu [a,b], Yan Zhou [a,b], Chao-Li Wang [a,b], Yong Liu [a,b,*], Duan-Jian Tao [a,b,*]

[a] College of Chemistry and Chemical Engineering, Jiangxi Normal University, Nanchang, Jiangxi 330022, China
[b] Henan Key Laboratory of Polyoxometalate Chemistry, College of Chemistry and Chemical Engineering, Henan University, Kaifeng, Henan 475004, China

ABSTRACT

Traditional processes for the synthesis N-OMCs as effective and bifunctional materials for CO_2 capture and oxygen reduction reaction (ORR) are unfavorable from the perspective of green chemistry. Herein, we reported the synthesis of N-OMCs through a solvent-free self-assembly route. A N-doped ordered mesoporous polymer (N-OMP) as the carbon precursor was first synthesized from manually mixed terephthalaldehyde, *m*-aminophenol and Pluronic F127. The precursors were then mechanically mixed with g-C_3N_4 for carbonization at different temperatures to result in a series of N-OMCs. The resultant N-OMCs were found to have well-developed ordered mesoporosity, and high nitrogen contents of 5.82–6.53 wt%. As a result, the CO_2 capacities of N-OMCs can reach as high as 2.46 mmol/g at 0 °C and 0.15 bar, and the adsorption of CO_2 by N-OMCs also shows high selectivities towards N_2 as well as excellent recycling performance. The ORR activity of N-OMCs is very impressive, with the onset potential of 1.003 V, and half-wave potential of 0.858 V. Overall, the ORR activity of N-OMCs is much better than that of commercial Pt/C catalyst.

1. Introduction

Fossil fuels such as petroleum, coal and natural gas have constituted the major source of energy for human and industrial activities over the past centuries [1]. The consumption of fossil fuels leads to a series of environmental issues, among which greenhouse effect is a most concerned one [2]. It is mainly caused by the accumulation of CO_2 in the atmosphere, and CO_2 is the major product of fossil fuels combustion. Greenhouse effect can prevent the thermal radiation from the earth to outer space, thus making the surface temperature of the earth constantly increased [3]. As a result, the elevating of see level and desertification of green lands occur, which impose significant threats to the surviving environment for livings on the earth. Therefore, the capture of CO_2 is of great importance to protect the surviving environment for livings on the earth.

Generally, the CO_2 capture methods can be divided into three types: absorption with liquid solvents [4], adsorption with solid materials [5], and separation with thin membranes [6]. Absorption with liquid solvents is the most widely investigated, and aqueous alkanolamines [7], ionic liquids (ILs) [8–10] and deep eutectic solvents (DESs) [11–15] are

common liquid solvents. However, aqueous alkanolamines have high volatility and strong corrosion, and the regeneration of them is highly energy-intensive. Although ILs and DESs have extremely low volatility, their viscosities are normally high which unfavors the transportation of them in pipelines. Separation with thin membranes is low in energy consumption, and beneficial for continuous operation. However, this method is still underdeveloped, and the production of membranes with large areas and robust mechanical strength remains to be addressed [16].

In comparison, adsorption with solid materials is a promising CO_2 capture method featuring low energy consumption, and free of volatile and corrosive issues. To date, a wide spectrum of solid materials has been developed for CO_2 capture, including zeolites [17,18], metal oxides [19–21], porous silicas [22,23], porous polymers [24–26], porous carbons [27–32], and metal–organic frameworks [33–35]. Among these materials, porous carbons are particularly attractive considering that they have high thermal stability, large surface areas, adjustable porosity and chemical structure, and can be synthesized from a wide range of precursors. For the application of porous carbons in CO_2 capture, it is necessary to construct ordered mesoporosity and abundant N species
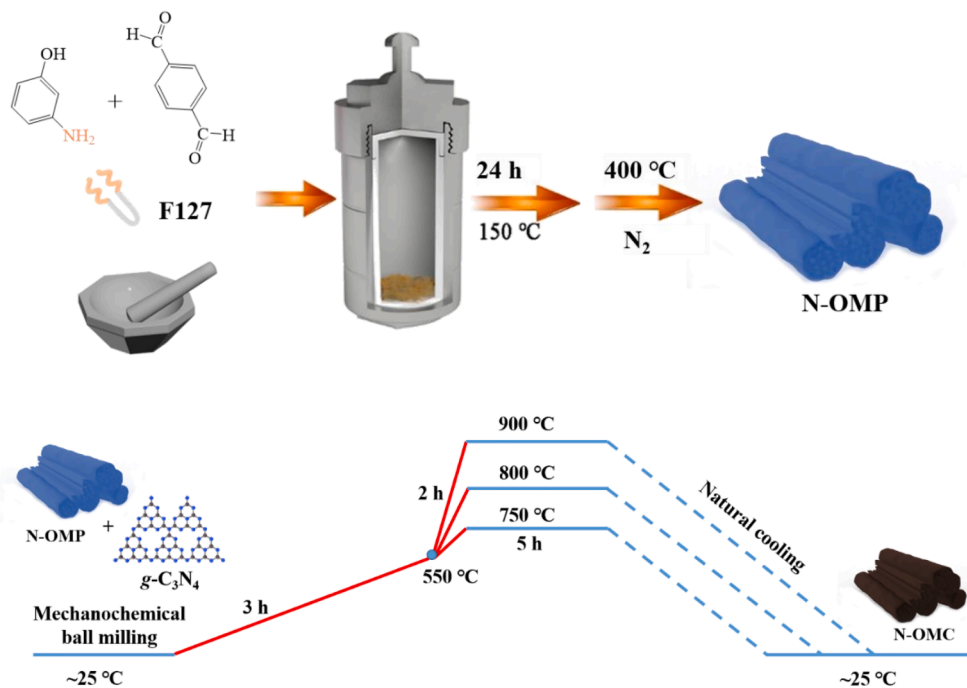

Fig. 1. Synthetic route of N-OMP and N-OMCs.

into the frameworks of porous carbons [36–38]. The ordered mesoporosity is favorable for the transportation of gas molecules, and the N species provide basic sites for selective binding with CO_2.

On the other hand, there is a strong demand for the exploration of clean energy sources, in view of the environmental issues caused by fossil fuels combustion. Within this regard, fuel cells are considered as promising candidates because they can produce renewable and clean electricity with high energy densities [39]. However, the oxygen reduction reaction (ORR) at the cathodes of fuel cells is normally sluggish, which hinders the development of fuel cells [40]. Although Pt-based electrocatalysts are well-known to be effective for the acceleration of ORR, they are difficult to be commercialized due to the high cost and poor stability of Pt [41]. It is necessary to develop effective electrocatalysts with low cost and good stability for the acceleration of ORR. Recently, ordered mesoporous carbons doped with heteroatoms (e.g., N, P, S and B) showed superior electrocatalytic activity for ORR [42].

Therefore, the synthesis of N-doped ordered mesoporous carbons (N-OMCs) as effective and bifunctional materials for CO_2 capture and ORR has become a hotspot of academic research. Traditionally, the ordered mesoporosity in porous carbons was constructed by solution-based template methods, in which soft [43,44] or hard [45] templates can be employed. However, the use of large-quantity solvents for materials synthesis is unfavorable from the perspective of green chemistry. Herein, we reported the synthesis of N-OMCs through a solvent-free self-assembly route, as shown in Fig. 1. A N-doped ordered mesoporous polymer (N-OMP) as the carbon precursor was first synthesized from manually mixed terephthalaldehyde, *m*-aminophenol and Pluronic F127. The precursors were then mechanically mixed with g-C_3N_4 for carbonization at different temperatures to result in a series of N-OMCs. Herein, g-C_3N_4 acts as the N source since the decomposition of it at high temperature releases large amounts of N-containing gases [46]. The resultant N-OMCs were then systematically characterized, and investigated for CO_2 capture performance and ORR activity.

2. Experimental

2.1. Chemicals

All the chemicals were of analytical grade and used directly without further purification. Terephthalaldehyde, *m*-aminophenol and Pluronic F127 ($M_w = 12600$) were purchased from Sigma-Aldrich. Urea (99 wt%) was obtained from Sinopharm. CO_2 (99.999 vol%) and N_2 (99.999 vol%) were supplied by Dalian Special Gas.

2.2. Synthesis

To synthesize N-OMP: 1.12 g of terephthalaldehyde, 0.88 g of *m*-aminophenol and 4.00 g of F127 were manually mixed and ground at room temperature; the mixture was then sealed in an autoclave and treated at 150 °C for 24 h; the resultant brown solid was transferred to a tube furnace, heated to 400 °C at 1 °C/min, and kept for 5 h in N_2 flow (10 mL/min) to remove the template; after cooling down to room temperature, a N-OMP was obtained. To synthesize g-C_3N_4: 5.00 g of urea was loaded in a tube furnace, heated to 550 °C at 5 °C/min, and kept for 2 h in air; after cooling down to room temperature, g-C_3N_4 was obtained. To synthesize N-OMCs: 1.00 g of N-OMP and 5.00 g of g-C_3N_4 were mechanically milled for 10–30 min at room temperature; the mixture was heated for 3 h to 550 °C, then for 5 h to 750, 800 or 900 °C, and finally kept for 2 h in N_2 flow (10 mL/min); after cooling down to room temperature, a series of N-OMCs were obtained. About 1.62 g of N-OMCs can be obtained from 1.00 g of N-OMP and 5.00 g of g-C_3N_4.

2.3. Characterizations

Before characterizations, the samples were pretreated under vacuum at 200 °C for 5 h. The N_2 isotherms at − 196 °C were measured by a Micromeritics 3Flex physisorption analyzer. The specific surface areas were obtained by the Brunauar-Emmett-Teller equation using the adsorption data in the relative pressure range of 0.05–0.20. The micropore volumes were obtained by the *t*-plot method using the adsorption data in the thickness range of 0.45–0.60. The total pore volumes were obtained according to the N_2 uptakes at the relative
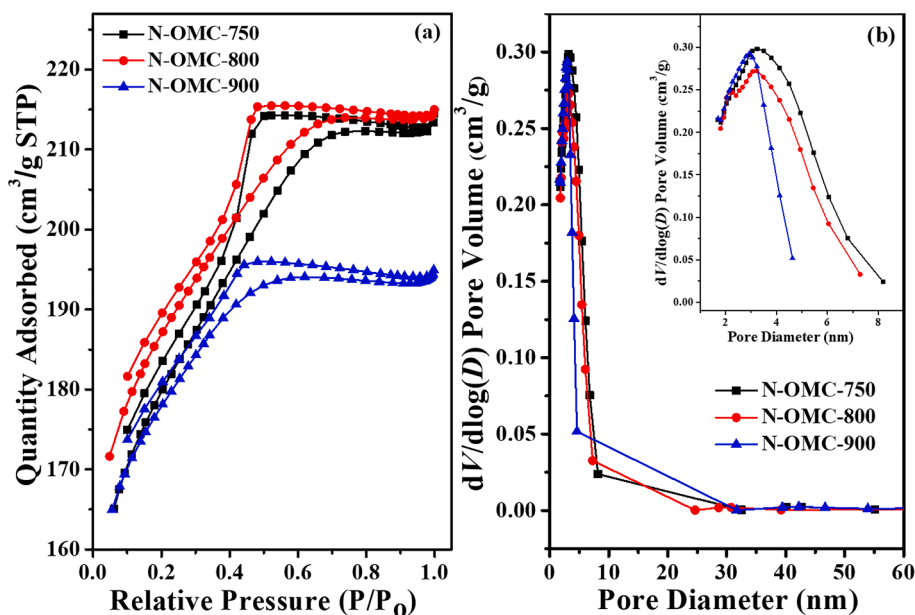
Fig. 2. N_2 isotherms at −196 °C (a) and pore width distributions (b) of synthesized N-OMCs.

pressure of 0.998. The pore width distributions were obtained by the Barrett-Joyner-Halenda (BJH) model using the desorption data. The total contents of N were measured by a Vario EL III elemental analyzer. The transmission electron microscopic (TEM) images were obtained by a Jeol JEM 2010EX microscope at 200 kV. The X-ray diffraction (XRD) patterns were collected on a Panalytical X'Pert powder diffractometer with Cu Kα radiation (λ = 1.5406 Å, 40 kV, 40 mA). The laser Raman spectra were collected on a Renishaw InVia Reflex spectrometer. The X-ray photoelectron spectroscopy (XPS) studies were performed on a Thermo ESCALAB 250 spectrometer with the binding energies corrected by C 1 s peak at 284.8 eV.

2.4. Gas adsorption

Before measurements, the samples were pretreated in N_2 flow (20 mL/min) at 150 °C for 12 h. The CO_2 and N_2 isotherms at 0 and 25 °C were measured by a Micromeritics Tristar II 3020 physisorption analyzer. The breakthrough curves of CO_2/N_2 mixed gas were measured by a Micromeritics AutoChem II chemisorption analyser ~100 mg of sample in 40 –60 mesh was fixed in a U-type quartz tube with an inner diameter of 0.8 cm. Since the bulk density of N-OMCs is very low, the packing volume of ~100 mg of sample is ~ 0.7 cm^3, corresponding to the packing height of 1.4 cm. Therefore, ~100 mg of sample is sufficient enough for the breakthrough experiments. The sample was stabilized in Ar flow (20 mL/min) at the target temperature for 1 h. The Ar flow was then changed to a CO_2/N_2 mixed gas flow, and the contents of CO_2 and N_2 in tail gas were measured online by a Hiden HPR-20 mass spectrometer. The CO_2/N_2 mixed gas was generated from pure CO_2 and N_2 by adjusting the mass flowmeters.

2.5. ORR activity tests

The ORR activity tests were carried out by a Chenhua CHI 760D electrochemical station equipped with an ALS RRDE-3A rotating ring disk electrode setup using a standard three-electrode cell. The modified rotating disk electrode (RDE) and rotating ring disk electrode (RRDE) were used as the working electrodes, while the Pt wire and saturated calomel electrode (SCE) as the counter and reference electrodes respectively. The experiments were performed in either O_2-saturated or N_2-saturated 0.1 M KOH solution at room temperature. To prepared the modified RDE, 3.5 mg of sample was dispersed in a mixture of 120 μL of

isopropanol, 370 μL of deionized water and 10 μL of Nafion solution (5 wt%, DuPont) by sonication for 30 min. Then, 4 μL of the dispersion was dropped onto the RDE (3 mm), and dried at room temperature to obtain the modified RDE, on which the loading of sample was 0.4 mg/cm^2. For comparison, the modified RDE with the same loading of commercial Pt/C (20 wt%, JM) was also prepared. All the potentials measured in this work were converted to the reversible hydrogen electrode (RHE) using the following equation:

$$E_{RHE} = E_{SCE} + 0.0591 \times pH + 0.241 \tag{1}$$

The ORR activity was evaluated by the cyclic voltammetry (CV) and linear sweep voltammetry (LSV) experiments. The CV experiments were performed between 1.1 and 0.3 V of relative RHE potential at a scanning rate of 50 mV/s. The LSV experiments were performed at a scanning rate of 10 mV/s and rotating rate of 400–2500 rpm. The potential of current–time (i-t) value was set to 0.8 V (vs. RHE). The electron transfer number (n) was determined by the Koutecky-Levich (K-L) equations:

$$\frac{1}{j} = \frac{1}{j_K} + \frac{1}{j_L} = \frac{1}{j_K} + \frac{1}{B\omega^{0.5}} \tag{2}$$

$$B = 0.62nFC_O(D_O)^{2/3}v^{-1/6} \tag{3}$$

$$j_K = nFkC_O \tag{4}$$

where j, j_k and j_L are the measured, kinetic-limited and diffusion-limited current densities respectively; ω is the angular velocity of the disk; n is the number of electrons transferred per O_2 molecule; F is the Faraday constant (96,500 C/mol); C_O and D_O are the concentration and diffusion coefficient of O_2 in 0.1 M KOH, which equal to 1.2×10^{-3} M and 1.9×10^{-5} cm^2/s respectively; v is the kinetic viscosity (0.01 cm^2/s); and k is the electron-transfer rate constant. For the experiments using RRDE as the working electrode, the voltage on Pt ring was 1.51 V (vs. RHE) at a scanning rate of 5 mV/s. Thus, the yield of H_2O_2 and electron transfer number n were calculated using the following equations:

$$n = \frac{4I_D}{I_D + (I_R/N)} \tag{5}$$

$$\backslash\% \ HH_2O_2 = 100 \times \frac{2I_R/N}{I_D + (I_R/N)} \tag{6}$$

The I_D is the disk current, I_R is the ring current, and $N = 0.424$ is the

Table 1

Porosity parameters and N contents of synthesized N-OMCs.

Sample	S_{BET} (m^2/g)[a]	V_m (cm^3/g)[b]	V_t (cm^3/g)[c]	D_n (nm)[d]	N (wt. %)[e]
N-OMC-750	562	0.18	0.32	3.0	6.53
N-OMC-800	580	0.20	0.32	2.9	6.32
N-OMC-900	553	0.19	0.29	2.5	5.82

[a] Specific surface area.
[b] Micropore volume.
[c] Total pore volume.
[d] Average pore width.
[e] N content.

collection efficiency of the Pt ring.

3. Results and discussion

3.1. Characterization results

The N-OMP was firstly characterized by low-temperature N_2 adsorption and SAXRD to confirm that it has well-ordered mesoporous structure (see Figs. S1–S2). Three N-OMCs with different carbonization temperatures were synthesized, and they were abbreviated as N-OMC-*T* (where *T* is the carbonization temperature). The porous structure of synthesized N-OMCs was examined by low-temperature N_2 adsorption first. Fig. 2 shows the N_2 isotherms at −196 °C and pore width distributions of N-OMCs. As can be seen, the N_2 uptakes first increase with the increase of relative pressures, but then keep almost unchanged with the further increase of relative pressures. There are minor hysteresis loops between the adsorption and desorption branches of N_2 isotherms.
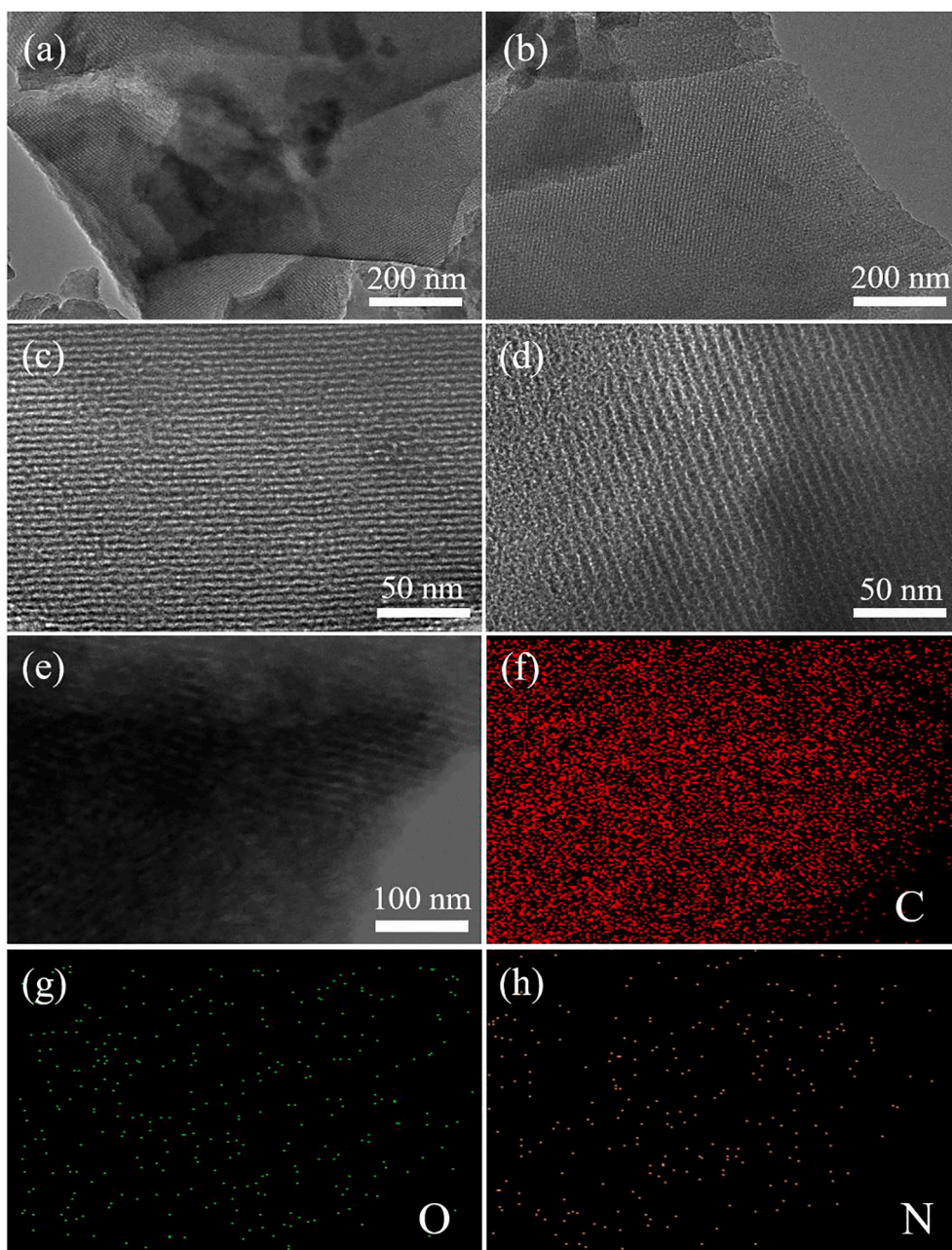

Fig. 3. TEM images (a–d), STEM image (e) and elemental mapping (f–h) of N-OMC-750.
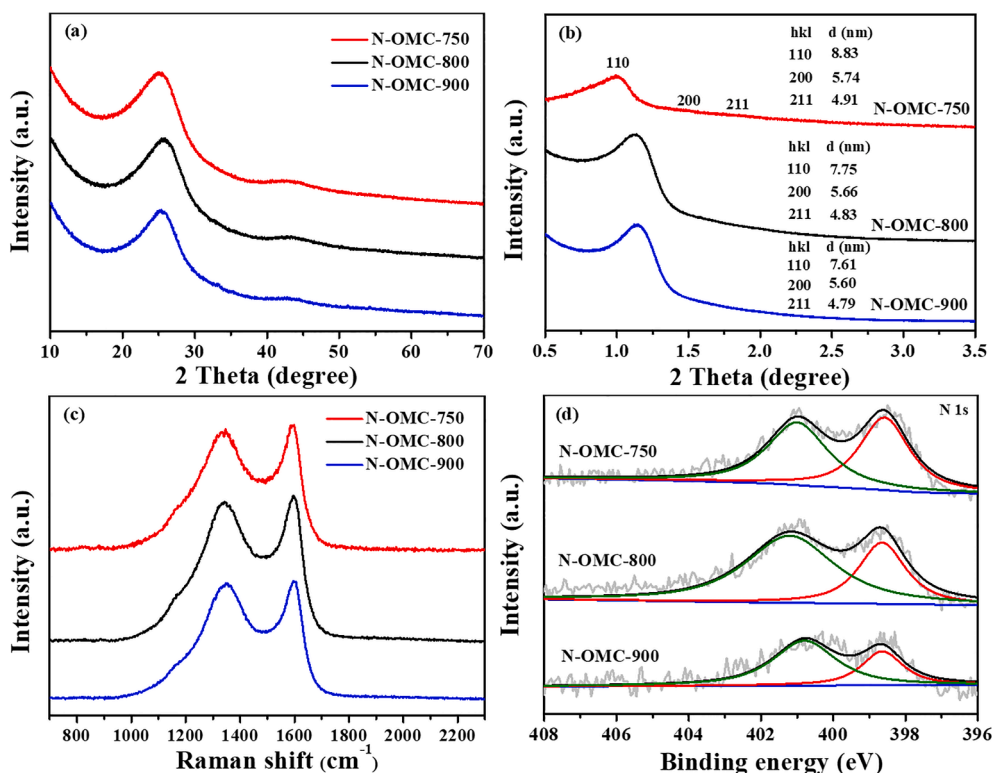
Fig. 4. WAXRD patterns (a), SAXRD patterns (b), Raman spectra (c) and XPS N 1s spectra of synthesized N-OMCs.

Obviously, the N_2 isotherms belong to type IV according to the IUPAC definitions, suggesting the predominantly mesoporous structure of N-OMCs. This can also be evidenced from the pore width distributions, which show considerable values for $dV/dlog(D)$ pore volumes in the mesopore range, and the largest values are centered at ~3 nm.

The porosity parameters of N-OMCs were calculated according to the N_2 adsorption or desorption data, and results are summarized in Table 1. It can be seen that the three N-OMCs have comparable porosity parameters, with the specific surface areas of 553–580 m^2/g, micropore volumes of 0.18–0.20 cm^3/g, total pore volumes of 0.29–0.32 cm^3/g, and average pore width of 2.8–3.2 nm. The porosity parameters of N-OMCs are not very high, because no any activation agents were used during the carbonization process. Actually, these values are common for N-OMCs prepared without activation agents [36–38]. According to the elemental analysis, the total contents of N in N-OMCs are 5.82–6.53 wt %, and decrease with the increase of carbonization temperatures. This is understandable since the loss of N species in porous carbons tends to be more significant at higher carbonization temperatures [47].

The morphology of synthesized N-OMCs was examined by electron microscope then. Fig. 3 shows the TEM images, STEM image and elemental mapping of N-OMC-750. As can be seen from the TEM images, there are abundant mesopores in N-OMC-750, and the mesopores are arranged in a highly ordered form. From the STEM image, the surface of N-OMC-750 shows rough characteristic, and highly ordered mesopores can also be clearly observed. The rough surface characteristic of N-OMC-750 can also be clearly observed from the SEM images (see Fig. S3). From the elemental mapping, there are abundant N atoms detected on the surface of N-OMC-750, and these N atoms are evenly distributed on the surface.

The crystalline structure of synthesized N-OMCs was examined by XRD subsequently. Fig. 4a and 4b show the WAXRD and SAXRD patterns of N-OMCs. As can be seen from the WAXRD patterns, there are two wide peaks at 24.9 and 43.4°, which can be assigned to the reflections of (0 0 2) and (1 0 0) lattices respectively. The two peaks indicate that N-OMCs have non-crystalline and amorphous structure on the whole. From

the SAXRD patterns, one strong peak is observed at ~1.0°, and two weak peaks are observed at ~1.5 and ~1.8°, which can be assigned to the reflections of (1 1 0), (2 0 0) and (2 1 1) lattices respectively. The three peaks indicate that the ordered mesopores of N-OMCs are arranged in a body-centered cubic form. It is noted that the *d*-spacing value of (1 1 0) lattices in N-OMC-750 is obviously larger than those of (1 1 0) lattices in N-OMC-800 and 900 (8.83 vs. 7.75 and 7.61 nm). This observation suggests that higher carbonization temperatures are favorable for the formation of N-OMCs with smaller unit cell parameters.

The bonding structure of synthesized N-OMCs was examined by Raman spectra as well, as shown in Fig. 4c. It can be seen that there are two peaks at 1345 and 1595 cm^{-1}, which can be assigned to the D and G bands respectively. The D and G bands are associated with sp^3-bonded carbon atoms in amorphous matrices and sp^2-bonded carbon atoms in graphitic matrices respectively. The intensities of D bands are comparable to those of G bands, suggesting the predominantly amorphous structure of N-OMCs, which agree well with the XRD results.

The nature of N species in synthesized N-OMCs was analyzed by XPS finally. The XPS survey and elemental compositions are presented in the Supplementary Material (see Fig. S4 and Table S1). There are three elements detected on the surface of N-OMCs: C, N and O. The atomic percentages of N are measured to be 4.0–6.3 at.%, and decrease with the increase of carbonization temperatures, which is consistent with the elemental analysis results. Fig. 4d shows the XPS N 1 s spectra of N-OMCs. The N 1 s spectra can be deconvoluted into two peaks at 398.6 and 401.0 eV, which can be assigned to the pyridinic and graphitic N respectively. It is noted that the percentages of pyridinic N decrease while those of graphitic N increase with the increase of carbonization temperatures (see Table S2). This observation suggests that higher carbonization temperatures are favorable for the formation of graphitic N on N-OMCs.

3.2. CO₂ capture performance

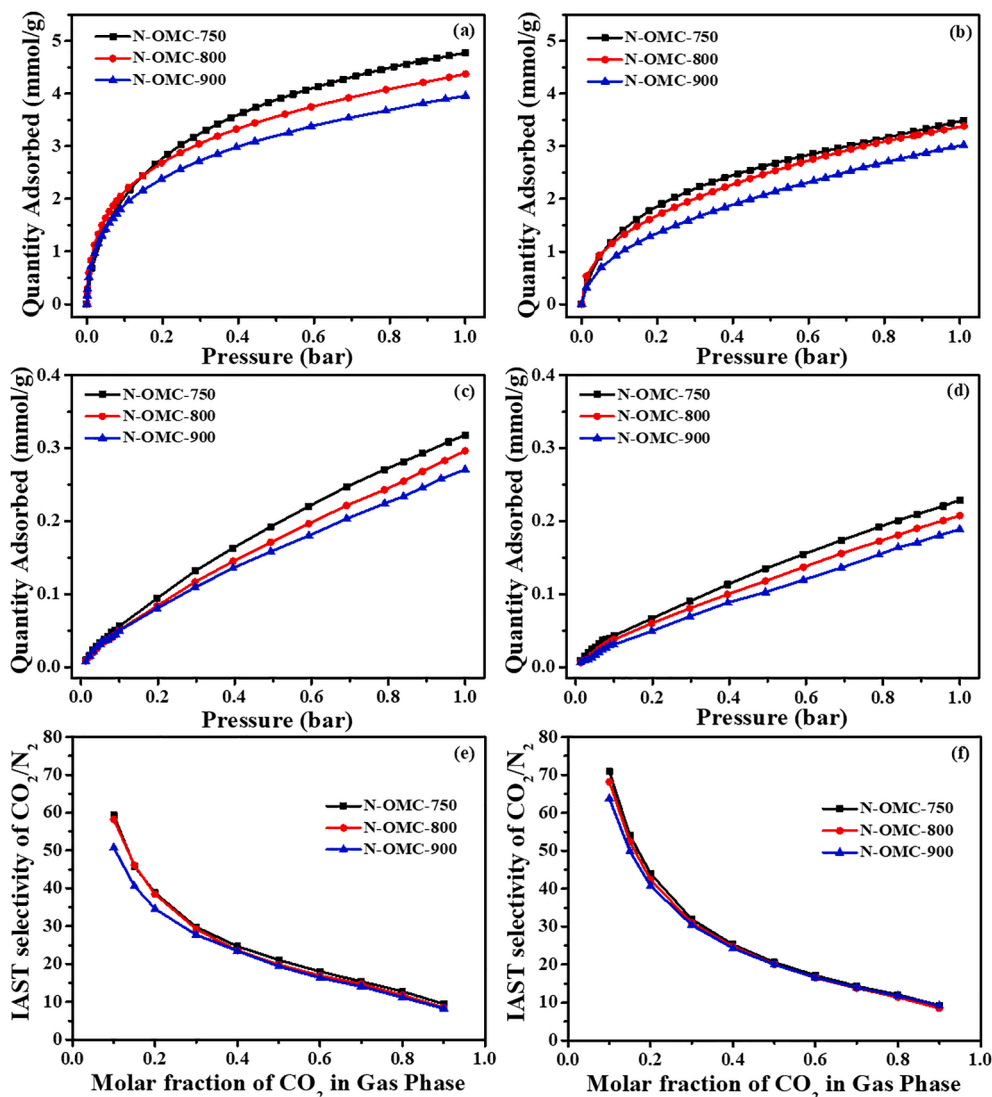The CO_2 capture performance of synthesized N-OMCs was examined

Fig. 5. CO_2 isotherms (a–b) and N_2 isotherms (c–d) of synthesized N-OMCs at 0 °C (a, c) and 25 °C (b, d); predicted IAST selectivities of synthesized N-OMCs for CO_2-N_2 mixtures at 0 °C and 1 bar (e); predicted IAST selectivities of synthesized N-OMCs for CO_2-N_2 mixtures at 25 °C and 1 bar (f).

by measuring the CO_2 adsorption capacities first. Fig. 5a and 5b show the CO_2 isotherms of N-OMCs at 0 and 25 °C, respectively. It can be seen that the CO_2 capacities increase with the increase of pressures in a non-linear form, suggesting that there exists strong interaction between N-OMCs and CO_2. Such interaction should arise from the pyridinic N on N-OMCs considering that pyridinic N has lone pair electrons. As a result, the CO_2 capacities of N-OMCs are very promising, especially at low pressures. For example, N-OMC-750 can adsorb 2.46 mmol/g of CO_2 at 0 °C and 0.15 bar. This is particularly relevant to the capture of CO_2 from the product of fossil fuels combustion, because the contents of CO_2 are normally low in the combustion product. The CO_2 capacities also decrease with the increase of temperatures, as a result of the exothermic nature of gas adsorption process [48,49]. For example, the CO_2 capacities of N-OMC-750 at 0.15 bar decrease from 2.46 to 1.64 mmol/g as the temperatures increase from 0 to 25 °C. Therefore, the CO_2-saturated N-OMCs can be regenerated at higher temperatures with the assistance of N_2 sweeping. There is no obvious loss in CO_2 capacities for N-OMCs in five times of repeated adsorption (see Fig. S5).

In addition, the CO_2 capacities of N-OMCs decrease with the increase of carbonization temperatures. For example, N-OMC-900 can adsorb only 2.17 mmol/g of CO_2 at 0 °C and 0.15 bar, and 1.17 mmol/g at 25 °C and 0.15 bar, which are lower than the CO_2 capacities of N-OMC-750

when compared at the same condition. Since the three N-OMCs have comparable porosity parameters, there are two factors contributing to this result. First, the total contents of N in N-OMCs decrease with the increase of carbonization temperatures (see Table 1). Second, the percentages of pyridinic N decrease with the increase of carbonization temperatures (see Table S2). As a result, the number of active sites in N-OMCs that enable strong interaction with CO_2 decreases with the increase of carbonization temperatures. To better understand the interactions of N-OMCs with CO_2, the CO_2 adsorption heats of N-OMCs were calculated by Clausius-Clapeyron equation using the CO_2 isotherms at 0 and 25 °C (see Fig. S6). It is found that the CO_2 adsorption heats of N-OMC-750 are in the range of 44.3–36.4 kJ/mol when the quantities adsorbed are 0.2–2.0 mmol/g. These values are slightly higher than those of other N-doped carbons reported in the literature [50,51]. In addition, the CO_2 adsorption heats of N-OMCs decrease with the increase of carbonization temperatures, which agrees well with the decreased active site numbers and CO_2 capacities of N-OMCs.

The CO_2 capture performance of synthesized N-OMCs was examined by measuring the N_2 adsorption capacities then. Fig. 5c and 5d show the CO_2 isotherms of N-OMCs at 0 and 25 °C respectively. As can be seen, the N_2 capacities increase with the increase of pressures almost in a linear form, suggesting that the interaction between N-OMCs and N_2 is very

Table 2

CO$_2$ capacities of synthesized N-OMCs at 0.15 bar and predicted IAST selectivities for CO$_2$-N$_2$ mixture (0.15:0.85) at 1 bar.

Sample	CO$_2$ capacity at 0.15 bar (mmol/g)		IAST selectivity of CO$_2$/N$_2$	
	0 °C	25 °C	0 °C	25 °C
N-OMC-750	2.46	1.64	46.1	54.0
N-OMC-800	2.45	1.50	45.8	52.3
N-OMC-900	2.17	1.17	40.6	49.8

weak. As a result, the N$_2$ capacities of N-OMCs are much lower than the CO$_2$ capacities. For example, N-OMC-750 can adsorb only 0.28 mmol/g of N$_2$ at 0 °C and 0.85 bar. This is very useful for the selective capture of CO$_2$ from the product of fossil fuels combustion, because there also exists large amount of residual N$_2$ in the combustion product.

With the CO$_2$ and N$_2$ capacities, the CO$_2$/N$_2$ selectivities of synthesized N-OMCs can be predicted by the ideal adsorption solution theory

(IAST) [52], as shown in Fig. 5e and 5f. It can be seen that the CO$_2$/N$_2$ selectivities of N-OMCs decrease with the increase of carbonization temperatures. This is because there are more active sites enabling strong interaction with CO$_2$ in N-OMCs prepared at lower carbonization temperatures (see Tables 1 and S2). However, the interaction between N-OMCs and N$_2$ is very weak. The CO$_2$/N$_2$ selectivities of N-OMCs also increase with the increase of temperatures. This is because the strong interaction between N-OMCs and CO$_2$ makes the decrease of CO$_2$ capacities with increasing temperatures less significant than the decrease of N$_2$ capacities (see Fig. 5a – 5d). Table 2 summarizes the CO$_2$ capacities of synthesized N-OMCs at 0.15 bar and predicted IAST selectivities for CO$_2$-N$_2$ mixture (0.15:0.85) at 1 bar. These values are promising in comparison with those of many other materials reported in the literature (see Table S3).

The CO$_2$ capture performance of synthesized N-OMCs was examined by measuring the breakthrough curves of CO$_2$/N$_2$ mixed gas finally. Fig. 6a shows the breakthrough curves of CO$_2$/N$_2$ mixed gas (15/85 vol
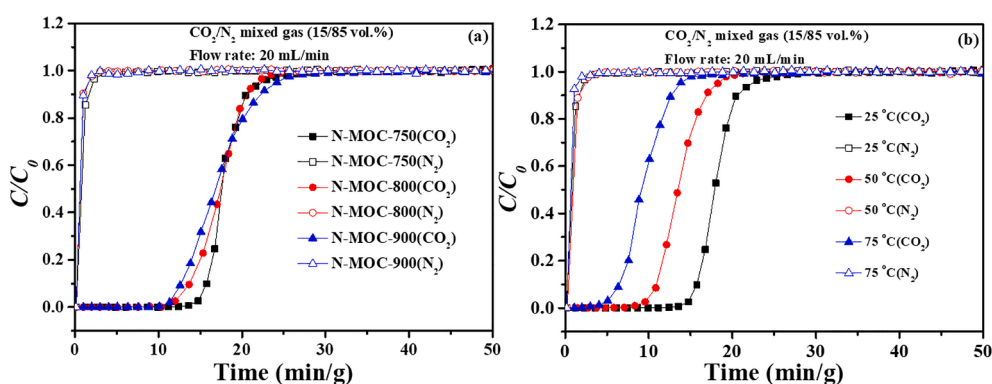

Fig. 6. Breakthrough curves of CO$_2$/N$_2$ mixed gas (15/85 vol%) adsorption by synthesized N-OMCs at 25 °C (a); breakthrough curves of CO$_2$/N$_2$ mixed gas (15/85 vol%) adsorption by N-OMC-750 at different temperatures (b).
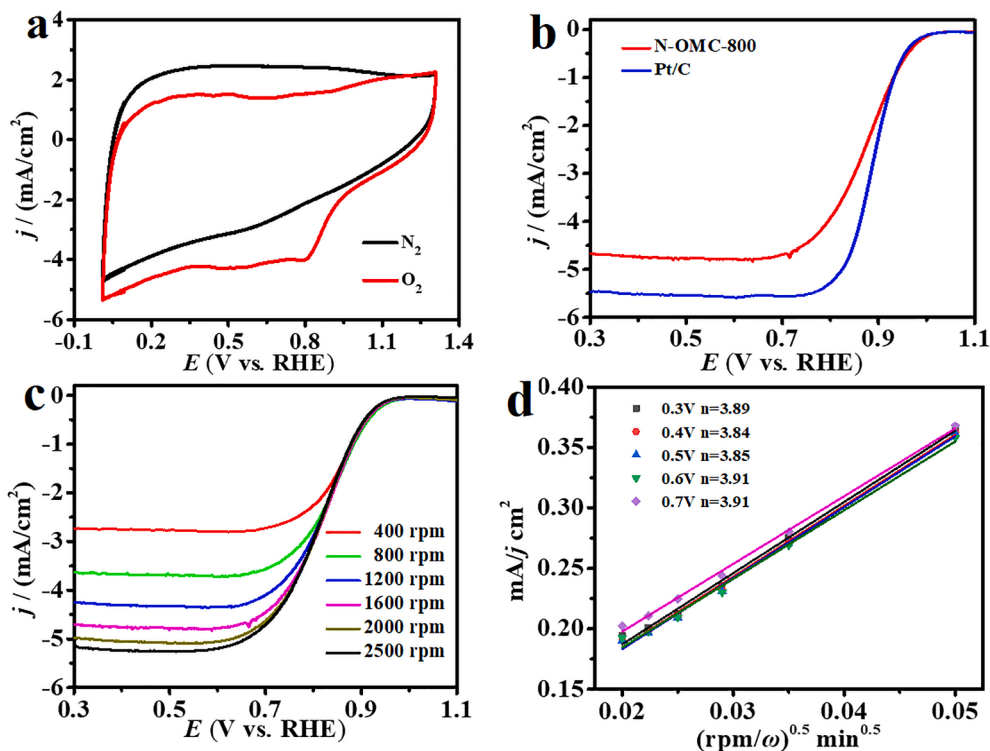

Fig. 7. CV curves of N-OMC-800 in N$_2$-and O$_2$-saturated 0.1 M KOH (a); LSV curves of N-OMC-800 and Pt/C in O$_2$-saturated 0.1 M KOH at a rotating rate of 1600 rpm (b); ORR curves of N-OMC-800 in O$_2$-saturated 0.1 M KOH at different rotating rates (c); K-L plots of j^{-1} vs. $\omega^{-0.5}$ for N-OMC-800 in O$_2$-saturated 0.1 M KOH (d).
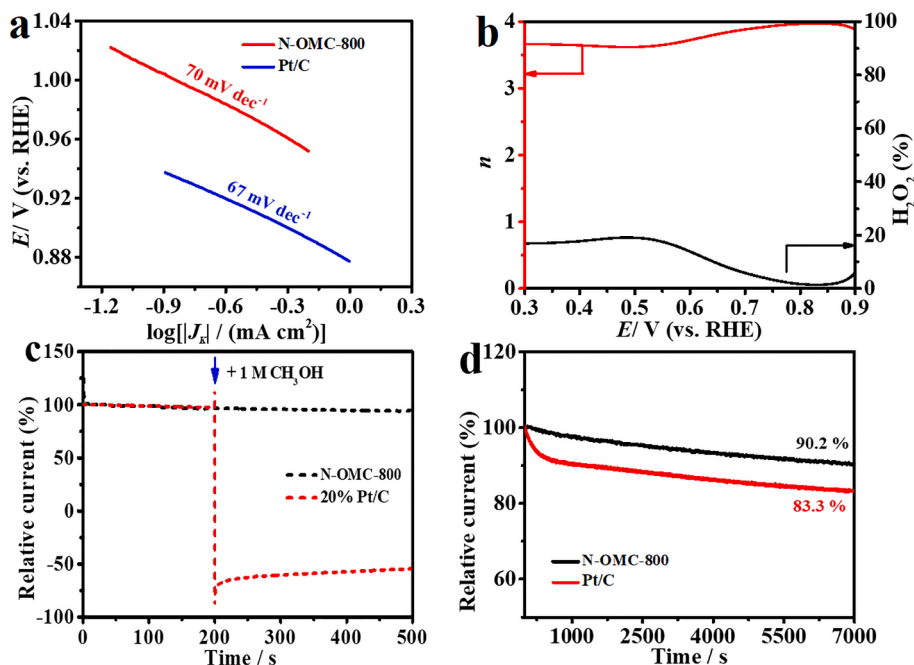
Fig. 8. Tafel plots for N-OMC-800 and Pt/C in 0.1 M KOH (a); electron transfer numbers (*n*) and corresponding yields of H_2O_2 for N-OMC-800 (b); chronoamperometric response of methanol crossover for N-OMC-800 and Pt/C at a rotating rate of 1600 rpm and 200 s after addition of methanol into O_2-saturated 0.1 KOH solution (c); durability test of N-OMC-800 and Pt/C for 7000 s in O_2-saturated 0.1 KOH (d).

%) adsorption by N-OMCs at 25 °C. As can be seen, the breakthrough of CO_2 starts at 10–15 min/g and completes at 25–30 min/g. However, the breakthrough of N_2 is much faster than that of CO_2, and completes almost instaneously. Therefore, N-OMCs can selectively adsorb CO_2 from N_2. The CO_2 capacities of breakthrough experiments can be estimated by integrating the breakthrough curves. The CO_2 capacities of N-OMC-750, N-OMC-800 and N-OMC-900 at 25 °C estimated from the breakthrough curves are 2.47, 2.38 and 2.24 mmol/g respectively. However, the CO_2 capacities of the three samples at 25 °C and 1 bar obtained from the isothermal measurements are 3.49, 3.38 and 3.02 mol/g respectively (see Fig. 5b). The CO_2 capacities estimated from the breakthrough curves are lower than those obtained from the isothermal measurements, because the competitive adsorption of N_2 partially decreases the adsorption of CO_2 in breakthrough experiments. Fig. 6b shows the breakthrough curves of CO_2/N_2 mixed gas (15/85 vol%) adsorption by N-OMC-750 at different temperatures. It can be seen that the breakthrough of CO_2 becomes faster as the temperatures increase. This is a result of the decreased CO_2 capacities at elevated temperatures (see Fig. 5a and 5b). Even though, the breakthrough of N_2 is still much faster than that of CO_2 at elevated temperatures. Therefore, the selective adsorption of CO_2 from N_2 by N-OMCs is still effective at elevated

temperatures. The efficiency for the selective adsorption of CO_2 from N_2 by N-OMCs can also be maintained in five times of repeated adsorption (see Fig. S7).

3.3. ORR activity

Herein, N-OMC-800 was selected as a representative of N-OMCs for the evaluation of ORR activity. The ORR activity was examined by performing the CV experiments in O_2-saturated and N_2-saturated 0.1 M KOH solution first and results are shown in Fig. 7a. N-OMC-800 displays high reduction reaction performance with a peak-current potential of 0.79 V in O_2-saturated 0.1 M KOH solution. However, no oxygen reduction peak can be observed in N_2-saturated solution, indicating that N-OMC-800 has oxygen reduction activity. The ORR activity was examined by performing the LSV experiments on RDE then. For comparison, the commercial Pt/C catalyst was also tested under the same condition. In Fig. 7b, the onset potential of N-OMC-800 is 1.003 V, which exceeds that of Pt/C (0.986 V). Meanwhile, N-OMC-800 possesses the half-wave potential ($E_{1/2}$) of 0.858 V, which is close to that of Pt/C (0.868 V). Furthermore, $E_{1/2}$ and E_{onset} of N-OMC-800 are superior to other different samples summarized in Table S4. This result validates
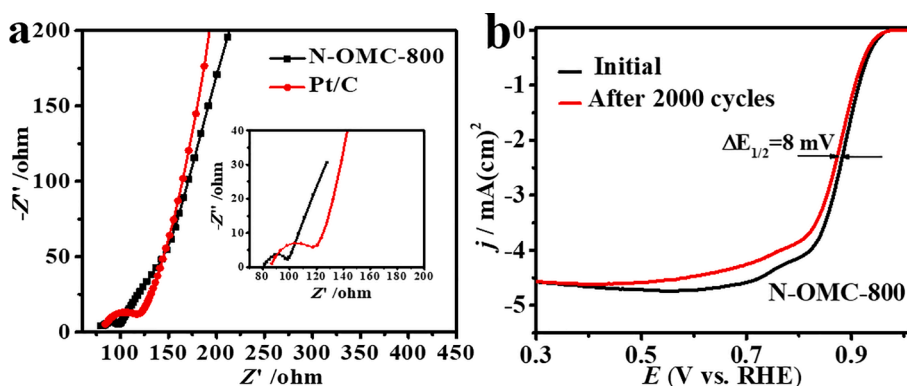

Fig. 9. Nyquist plots of N-OMC-800 and Pt/C in O_2-saturated 0.1 M KOH solution (a); LSV curves of N-OMC-800 before and after 2000 CV cycles (b)

that N-OMC-800 has high ORR activity. The RDE polarization curves at 400–2500 rpm were obtained to gain better insight into the kinetic parameters of ORR. Fig. 7c shows that increasing the rotation rates of N-OMC-800 electrode results in the increase of current densities, because the higher rotation rates are beneficial for the diffusion of electrolytes. In addition, the corresponding K-L plots were displayed in Fig. 7d, which display excellent linearity and parallelism, conforming to the first-order reaction kinetics for ORR. The average electron transfer number was calculated to be ~3.88 in the range of 0.3–0.7 V, suggesting a $4e^-$−dominant ORR pathway.

To better understand the kinetic properties of N-OMC-800, the Tafel plots were also obtained. As shown in Fig. 8a, the Tafel slope of N-OMC-800 was calculated to be 70 mV/dec2^{-1}, which is comparable to that of Pt/C (67 mV/dec). The yields of H_2O_2 on N-OMC-800 were then measured by using the RRDE. As expected, only a small amount of peroxide was generated during the reaction. The electron transfer numbers were estimated to be 3.66–3.96, further validating the $4e^-$−transfer process during the ORR (see Fig. 8b). The methanol tolerance and long-term cycling stability of electrocatalysts are also very important. Therefore, the methanol tolerance and long-term cycling stability of N-OMC-800 were examined by chronoamperometry. As shown in Fig. 8c, N-OMC-800 shows outstanding methanol tolerance. However, there is obvious methanol poisoning for Pt/C. It can also be found that N-OMC-800 has better long-time stability than Pt/C (see Fig. 8d). N-OMC-800 can preserve 90.2% of the current even after 7000 s of continuous testing, while Pt/C can preserve only 83.3% of the current.

The impedance spectroscopy measurements were then performed for N-OMC-800 and Pt/C in O_2-saturated 0.1 M KOH solution, and Fig. 9a shows the Nyquist plots. It can be seen that N-OMC-800 displays a smaller semicircle diameter than Pt/C in high frequency region, indicating the faster rate of charge transfer for the ORR reactions on N-OMC-800. The stability of ORR system was finally evaluated by accelerated durability tests (ADTs). It can be seen from Fig. 9b that the negative shift of $E_{1/2}$ is only 8 mV for N-OMC-800 after 2000 potential cycles. Furthermore, N-OMC-800 can preserve 90.2% of the current even after 7000 s of continuous testing, while Pt/C can preserve only 83.3% of the current from the chronoamperometry measurements (see Fig. 9d). These results indicate that N-OMC-800 is a stable catalyst for ORR reactions.

4. Conclusions

In summary, a series of N-OMCs were synthesized by a solvent-free self-assembly route, using terephthalaldehyde, *m*-aminophenol and Pluronic F127 as the starting chemicals, and g-C_3N_4 as the additional N source. The resultant N-OMCs were systematically characterized, and investigated for CO_2 capture performance and ORR activity. It is validated that the synthesized N-OMCs have well-developed ordered mesoporosity and high N contents. Therefore, the synthesized N-OMCs show promising CO_2 capture performance in comparison with many other materials reported in the literature. The synthesized N-OMCs also exhibit impressive ORR activity in comparison with commercial Pt/C catalysts. This work presents a new way for the fast and green synthesis of N-OMCs as effective and bifunctional materials for CO_2 capture and ORR.

Declaration of Competing Interest

The authors declare that they have no known competing financial interests or personal relationships that could have appeared to influence the work reported in this paper.

Acknowledgements

Appendix A. Supplementary data

References

[1] Y. Ma, R. Liang, W. Wu, J. Zhang, Y. Cao, K. Huang, L. Jiang, Enhancing the activity of MoS_2/SiO_2-Al_2O_3 bifunctional catalysts for suspended-bed hydrocracking of heavy oils by doping with Zr atoms, Chin. J. Chem. Eng. (2021), https://doi.org/10.1016/j.cjche.2021.03.015.

[2] J.F.B. Mitchell, The "greenhouse" effcet and climate change, Rev. Geophy. 27 (1989) 115–139.

[3] W.R. Cline, Scientific basis for the greenhouse effect, Econ. J. 101 (407) (1991) 904, https://doi.org/10.2307/2233863.

[4] C.-H. Yu, C.-H. Huang, C.-S. Tan, A review of CO_2 capture by absorption and adsorption, Aerosol Air Qual. Res. 12 (2012) 745–769.

[5] A.L. Chaffee, G.P. Knowles, Z. Liang, J. Zhang, P. Xiao, P.A. Webley, CO_2 capture by adsorption: materials and process development, Int. J. Greenh. Gas Control 1 (1) (2007) 11–18.

[6] P. Luis, T. Van Gerven, B. Van der Bruggen, Recent developments in membrane-based technologies for CO_2 capture, Prog. Energy Combust. Sci. 38 (3) (2012) 419–448.

[7] G.T. Rochelle, Amine scrubbing for CO_2 capture, Science 325 (5948) (2009) 1652–1654.

[8] G.K. Cui, J.J. Wang, S.J. Zhang, Active chemisorption sites in functionalized ionic liquids for carbon capture, Chem. Soc. Rev. 45 (2016) 4307–4339.

[9] F.F. Chen, K. Huang, J.P. Fan, D.J. Tao, Chemical solvent in chemical solvent: a class of hybrid materials for effective capture of CO_2, AIChE J. 64 (2018) 632–639.

[10] F. Liu, K. Huang, L. Jiang, Promoted adsorption of CO_2 on amine-impregnated adsorbents by functionalized ionic liquids, AIChE J. 64 (10) (2018) 3671–3680.

[11] F. Liu, W. Chen, J. Mi, J.-Y. Zhang, X. Kan, F.-Y. Zhong, K. Huang, A.-M. Zheng, L. Jiang, Thermodynamic and molecular insights into the absorption of H_2S, CO_2, and CH_4 in choline chloride plus urea mixtures, AIChE J. 65 (5) (2019) e16574, https://doi.org/10.1002/aic.v65.510.1002/aic.16574.

[12] H. Yan, L. Zhao, Y. Bai, F. Li, H. Dong, H. Wang, X. Zhang, S. Zeng, Superbase ionic liquid-based deep eutectic solvents for improving CO_2 absorption, ACS Sustain. Chem. Eng. 8 (6) (2020) 2523–2530.

[13] W.J. Jiang, F.Y. Zhong, L.S. Zhou, H.L. Peng, J.P. Fan, K. Huang, Chemical dual-site capture of NH_3 by unprecedently low-viscosity deep eutectic solvents, Chem. Commun. 56 (2020) 2399–2402.

[14] Y. Ma, J. Zhang, K. Huang, L. Jiang, Highly efficient and selective separation of ammonia by deep eutectic solvents through cooperative acid-base and strong hydrogen-bond interaction, J. Mol. Liq. 337 (2021) 116463, https://doi.org/10.1016/j.molliq.2021.116463.

[15] Y. Cao, J. Zhang, Y. Ma, W. Wu, K. Huang, L. Jiang, Designing low-viscosity deep eutectic solvents with multiple weak-acidic groups for ammonia separation, ACS Sustain. Chem. Eng. 9 (21) (2021) 7352–7360, https://doi.org/10.1021/acssuschemeng.1c0167410.1021/acssuschemeng.1c01674.s001.

[16] E. Favre, Membrane processes and postcombustion carbon dioxide capture: challenges and prospects, Chem. Eng. J. 171 (2011) 782–793.

[17] S.J. Chen, M. Zhu, Y. Fu, Y.X. Huang, Z.C. Tao, W.L. Li, Using 13X, LiX, and LiPdAgX zeolites for CO_2 capture from post-combustion flue gas, Appl. Energy 191 (2017) 87–98.

[18] R. Krishna, J.M. van Baten, A comparison of the CO_2 capture characteristics of zeolites and metal–organic frameworks, Sep. Purif. Technol. 87 (2012) 120–126.

[19] S.I. Garcés-Polo, J. Villarroel-Rocha, K. Sapag, S.A. Korili, A. Gil, Adsorption of CO_2 on mixed oxides derived from hydrotalcites at several temperatures and high pressures, Chem. Eng. J. 332 (2018) 24–32.

[20] M. Li, K. Huang, J.A. Schott, Z. Wu, S. Dai, Effect of metal oxides modification on CO_2 adsorption performance over mesoporous carbon, Micro. Meso. Mat. 249 (2017) 34–41.

[21] S. Wang, S. Yan, X. Ma, J. Gong, Recent advances in capture of carbon dioxide using alkali-metal-based oxides, Energy Environ. Sci. 4 (10) (2011) 3805, https://doi.org/10.1039/c1ee01116b.

[22] S. Yang, L. Zhan, X. Xu, Y. Wang, L. Ling, X. Feng, Graphene-based porous silica sheets impregnated with polyethyleneimine for superior CO_2 capture, Adv. Mater. 25 (15) (2013) 2130–2134.

[23] G. Zhang, P. Zhao, Y. Xu, Z. Yang, H. Cheng, Y. Zhang, Structure property-CO_2 capture performance relations of amine-functionalized porous silica composite adsorbents, ACS Appl. Mater. Inter. 10 (40) (2018) 34340–34354.

[24] K. Huang, F. Liu, L. Jiang, S. Dai, Aqueous and Template-free synthesis of meso-macroporous polymers for highly selective capture and conversion of carbon dioxide, ChemSusChem 10 (21) (2017) 4144–4149.

[25] K. Huang, J.-Y. Zhang, F. Liu, S. Dai, Synthesis of porous polymeric catalysts for the conversion of carbon dioxide, ACS Catal. 8 (10) (2018) 9079–9102.

[26] Y. Zeng, R. Zou, Y. Zhao, Covalent organic frameworks for CO_2 capture, Adv. Mater. 28 (15) (2016) 2855–2873.

[27] K. Huang, F. Liu, J.-P. Fan, S. Dai, Open and hierarchical carbon framework with ultralarge pore volume for efficient capture of carbon dioxide, ACS Appl. Mater. Inter. 10 (43) (2018) 36961–36968.

[28] H.-L. Peng, J.-B. Zhang, J.-Y. Zhang, F.-Y. Zhong, P.-K. Wu, K. Huang, J.-P. Fan, F. Liu, Chitosan-derived mesoporous carbon with ultrahigh pore volume for amine

impregnation and highly efficient CO_2 capture, Chem. Eng. J. 359 (2019) 1159–1165.

[29] Z. Wang, N.T. Goyal, L.Y. Liu, D.C.W. Tsang, J. Shang, W.J. Liu, G. Li, N-doped porous carbon derived from polypyrrole for CO_2 capture from humid flue gases, Chem. Eng. J. 396 (2020), 125376.

[30] S.F. Liu, L.L. Rao, P.P. Yang, X.Y. Wang, L.L. Wang, R. Ma, L.M. Yue, X. Hu, Superior $CO2$ uptake on nitrogen doped carbonaceous adsorbents from commercial phenolic resin, J. Environ. Sci. 93 (2020) 109–116.

[31] P.P. Yang, L.L. Rao, W.Q. Zhu, L.L. Wang, R. Ma, F.Y. Chen, G.R. Lin, X. Hu, Porous carbons derived from sustainable biomass via a facile one-step synthesis strategy as efficient CO_2 adsorbents, Ind. Eng. Chem. Res. 59 (2020) 6194–6201.

[32] L.Y. An, S.F. Liu, L.L. Wang, J.Y. Wu, Z.Z. Wu, C.D. Ma, Q.K. Yu, X. Hu, Novel nitrogen-doped porous carbons derived from graphene for effective $CO2$ capture, Ind. Eng. Chem. Res. 58 (2019) 3349–3358.

[33] Y. Jiang, P. Tan, S.C. Qi, X.Q. Liu, J.H. Yan, F. Fan, L.B. Sun, Metal-Organic Frameworks with target-specific active sites switched by photoresponsive motifs: efficient adsorbents for tailorable CO_2 capture, Angew. Chem. Int. Ed. l 58 (2019) 6600–6604.

[34] Y.C. Lin, C.L. Kong, Q.J. Zhang, L. Chen, Metal-organic frameworks for carbon dioxide capture and methane storage, Adv. Energy Mater. 7 (2017) 1601296.

[35] J. Liu, Y. Wei, Y. Zhao, Trace carbon dioxide capture by metal-organic frameworks, ACS Sustain. Chem. Eng. 7 (1) (2019) 82–93.

[36] G. Durá, V.L. Budarin, J.A. Castro-Osma, P.S. Shuttleworth, S.C.Z. Quek, J.H. Clark, M. North, Importance of micropore-mesopore interfaces in carbon dioxide capture by carbon-based materials, Angew. Chem. Int. Ed. 55 (32) (2016) 9173–9177.

[37] J.H. Lee, H.J. Lee, S.Y. Lim, B.G. Kim, J.W. Choi, Combined CO_2-philicity and ordered mesoporosity for highly selective CO_2 capture at high temperatures, J. Am. Chem. Soc. 137 (22) (2015) 7210–7216.

[38] F.J. Liu, K. Huang, Q. Wu, S. Dai, Solvent-free self-assembly to the synthesis of nitrogen-doped ordered mesoporous polymers for highly selective capture and conversion of CO_2, Adv. Mater. 29 (2017) 1700445.

[39] O.Z. Sharaf, M.F. Orhan, An overview of fuel cell technology: fundamentals and applications, Renew. Sust. Energ. Rev. 32 (2014) 810–853.

[40] J.K. Nørskov, J. Rossmeisl, A. Logadottir, L. Lindqvist, J.R. Kitchin, T. Bligaard, H. Jónsson, Origin of the overpotential for oxygen reduction at a fuel-cell cathode, J. Phys. Chem. B 108 (46) (2004) 17886–17892.

[41] F. Jaouen, E. Proietti, M. Lefèvre, R. Chenitz, J.-P. Dodelet, G. Wu, H.T. Chung, C. M. Johnston, P. Zelenay, Recent advances in non-precious metal catalysis for oxygen-reduction reaction in polymer electrolyte fuelcells, Energy Environ. Sci. 4 (1) (2011) 114–130.

[42] K. Wan, G.F. Long, M.Y. Liu, L. Du, Z.X. Liang, P. Tsiakaras, Nitrogen-doped ordered mesoporous carbon: synthesis and active sites for electrocatalysis of oxygen reduction reaction, Appl. Catal. B-Environ. 165 (2015) 566–571.

[43] J. Zhao, Y. Shu, P. Zhang, Solid-state CTAB-assisted synthesis of mesoporous Fe_3O_4 and $Au@Fe_3O_4$ by mechanochemistry, Chin. J. Catal. 40 (7) (2019) 1078–1084.

[44] L. Chuenchom, R. Kraehnert, B.M. Smarsly, Recent progress in soft-templating of porous carbon materials, Soft Matter 8 (42) (2012) 10801, https://doi.org/10.1039/c2sm07448f.

[45] J.S. Shi, H.M. Cui, J.G. Xu, N.F. Yan, Y.W. Liu, Design and fabrication of hierarchically porous carbon frameworks with Fe_2O_3 cubes as hard template for CO_2 adsorption, Chem. Eng. J. 389 (2020), 124459.

[46] J.Y. Zhang, J.B. Zhang, M.J. Li, Z.L. Wu, S. Dai, K. Huang, Solvent-free and one-pot synthesis of ultramicroporous carbons with ultrahigh nitrogen contents for sulfur dioxide capture, Chem. Eng. J. 391 (2020), 123579.

[47] M. Sevilla, P. Valle-Vigón, A.B. Fuertes, N-Doped polypyrrole-based porous carbons for CO_2 capture, Adv. Funct. Mater. 21 (14) (2011) 2781–2787.

[48] F. Liu, K. Huang, C.-J. Yoo, C. Okonkwo, D.-J. Tao, C.W. Jones, S. Dai, Facilely synthesized meso-macroporous polymer as support of poly(ethyleneimine) for highly efficient and selective capture of CO_2, Chem. Eng. J. 314 (2017) 466–476.

[49] Y. Han, W.S.W. Ho, Polymeric membranes for CO_2 separation and capture, J. Membr. Sci. 628 (2021), 119244.

[50] L.L. Rao, R. Ma, S.F. Liu, L.L. Wang, Z.Z. Wu, J. Yang, X. Hu, Nitrogen enriched porous carbons from d-glucose with excellent CO_2 capture performance, Chem. Eng. J. 362 (2019) 794–801.

[51] Y.Y. Zhan, Q.Q. Han, S.F. Pan, X. Kan, J.X. Mi, F.J. Liu, Y.N. Cao, C.T. Au, L. L. Jiang, Biomass-derived hierarchically porous carbons abundantly decorated with nitrogen sites for efficient co_2 catalytic utilization, Ind. Eng. Chem. Res. 58 (2019) 7980–7988.

[52] A.L. Myers, J.M. Prausnitz, Thermodynamics of mixed-gas adsorption, AIChE J. 11 (1) (1965) 121–127.